Article:
Nisar, L., Kusdhany, M.I.M., Nishihara, M. et al. (6 more authors) (2025) Probing charge trapping sites in M-N-C electrocatalysts via time-resolved transient absorption spectroscopy. Journal of Materials Chemistry A. ISSN 2050-7488

https://doi.org/10.1039/d5ta02913a

Journal of Materials Chemistry A

ROYAL SOCIETY OF CHEMISTRY

PAPER

View Article Online
View Journal

Cite this: DOI: 10.1039/d5ta02913a

Probing charge trapping sites in M–N–C electrocatalysts *via* time-resolved transient absorption spectroscopy†

Laraib Nisar, [a] Muhammad Irfan Maulana Kusdhany,[b] Masamichi Nishihara,[bc] Fayyaz Hussain, [d] Andrew D. Burnett, [e] Stephen Matthew Lyth,*[cf] Mohamed Pourkashanian,[g] Mohammed S. Ismail*[h] and Adrien A. P. Chauvet *[a]

Among non-platinum group metal (non-PGM) electrocatalysts for the oxygen reduction reaction (ORR), the class of metal-decorated nitrogen-doped carbon (M–N–C) materials is most promising. The active site is generally accepted to be a metal coordinated with nitrogen within the carbon lattice and/or nanoparticles. But confusion remains around the catalytic mechanisms. Better and more fundamental insights into these materials allow the design of more efficient M–N–C catalysts. In this study, we report the first direct observation of charge-trapping sites induced by metal decoration in M–N–C electrocatalysts using ultrafast time-resolved transient absorption spectroscopy. Ultrafast time-resolved spectroscopy has long been used for molecular characterization and to study photocatalysts, but its application to probe the intrinsic properties of electrocatalysts can be extended to all materials. Such sites have been associated with modulated charge distribution and enhancement of electron transfer efficiency during catalytic processes. Our study not only provides new insights into the electronic behavior of M–N–C materials but also establishes ultrafast spectroscopy as a powerful tool to study charge dynamics in electrocatalysts broadly, paving the way for more informed and efficient catalyst design.

Received 12th April 2025
Accepted 24th July 2025

DOI: 10.1039/d5ta02913a

rsc.li/materials-a

Introduction

Electrochemical energy storage and conversion technologies such as metal-air batteries and polymer electrolyte fuel cells (PEFCs) are expected to play a crucial role in the decarbonization of our societies. The oxygen reduction reaction (ORR) is a fundamental process in both of these technologies, occurring at the cathode.[1–3] However, the ORR suffers from relatively sluggish reaction kinetics, necessitating the use of an electrocatalyst to minimize activation overpotentials during device operation. Currently, platinum-based nanoparticles decorated on carbon supports are considered to be the state-of-the-art catalyst for the ORR, and are widely used in the commercial applications.[4–7] However, platinum-group metals (PGMs) are classed as critical raw materials (CRMs) due to their economic importance and scarcity, putting supply chains at risk and potentially limiting the commercialization of new technologies.[8] Therefore, extensive research efforts are underway to reduce catalyst loadings, recycle catalyst materials, or replace PGMs with non-PGM electrocatalysts for the ORR.[9–11]

Over the past decade, significant research has been conducted on non-PGM electrocatalysts. Carbon-based catalysts have emerged as a promising candidate due to the high electrical conductivity, low cost and large surface area of carbon, as well as the ease at which it can be decorated or doped with heteroatoms.[12,13] Pristine carbon is not particularly ORR active, and so it is generally doped with nitrogen to improve activity.[14,15] Furthermore, it has been determined that the presence of transition metal atoms (such as Fe, Co and Ni) coordinated to nitrogen atoms in a carbon matrix may result in promising ORR activity comparable to traditional PGM nanoparticles, and such materials are referred as M–N–C electrocatalysts.[16–20] The ORR activity of such electrocatalysts has been attributed to the synergistic combination of nitrogen doping and transition metal incorporation in carbon. In

[a]Dainton Building, Department of Chemistry, The University of Sheffield, Brook Hill, Sheffield, South Yorkshire S3 7HF, UK. E-mail: a.chauvet@sheffield.ac.uk

[b]Department of Automotive Science, Graduate School of Integrated Frontier Sciences, Kyushu University, 744 Motooka, Nishi-ku, Fukuoka 819-0395, Japan

[c]Next-Generation Fuel Cell Research Center (NEXT-FC), Kyushu University, 744 Motooka, Nishi-ku, Fukuoka 819-0395, Japan

[d]Materials Research Simulation Laboratory, Institute of Physics Bahauddin Zakariya University Multan, Pakistan

[e]School of Chemistry, University of Leeds, Woodhouse Lane, Leeds LS2 9JT, UK

[f]Strathclyde Incubator for Green Hydrogen Technologies (SigH$_2$t), Department of Chemical and Process Engineering, University of Strathclyde, 75 Montrose St, Glasgow G1 1XL, UK. E-mail: stephen.lyth@strath.ac.uk

[g]Translational Energy Research Center, The University of Sheffield, Sheffield, UK

[h]School of Engineering, University of Hull, Hull, HU6 7RX, UK. E-mail: m.ismail@hull.ac.uk

† Electronic supplementary information (ESI) available. See DOI: https://doi.org/10.1039/d5ta02913a

particular, the presence of nitrogen groups is expected to increase electron density on the carbon surface, facilitating electron transfer at the transition metal site during the ORR.[21,22] As such, it may be possible to tune the electronic configurations of M–N–C catalysts, enabling precise modulation of their electrocatalytic performance.

Meanwhile, other p-block heteroatoms such as boron,[23–25] sulfur,[26,27] and phosphorus[28–30] have also been investigated as alternative dopants or co-dopants with nitrogen. Such heteroatoms are reported to modify the electronic structure of the active site in a similar manner to nitrogen, by modifying the electron density. Among these, phosphorus has garnered attention due to its nitrogen-like electronic configuration, and much work has focused on developing N and P co-doped supports that could offer stronger interactions with the transition metal active site center.[31,32] The key reasoning behind the doping strategies is to enhance the availability of electrons at the catalyst–support interface. By increasing electron density at the catalyst surface, doped carbon supports are expected to facilitate charge transfer between the support and the metal sites, potentially leading to enhanced electrocatalytic performance.

Whilst it is theorized that metal introduction enhances charge transport (and therefore catalytic activity) in M–N–C electrocatalysts, direct experimental proof for this mechanism is still limited. Various theories regarding modification of the electronic structure have been proposed to explain the activity of such electrocatalysts for the ORR. For example, Lee *et al.* demonstrated that an excess electron reservoir in catalyst support can enhance the efficiency of water electrolysis by facilitating charge replenishment.[33] In another study, Jiang *et al.* demonstrated that *in situ* tuning of platinum 5d valence states can dynamically control charge transfer, thereby enhancing the activity and selectivity of catalysts for ORR.[34] However, much of the evidence to date relies on indirect measurements or theoretical models.

In this study, we employ ultrafast transient absorption spectroscopy (TAS) for the first time to investigate the intrinsic properties of materials designed for ORR. TAS is a powerful technique used to study the dynamic electronic and nuclear processes occurring in materials on femtosecond to nanosecond timescales.[35] By employing an ultrafast laser pulse (the "pump") to excite a system, generate free high-energy electrons, and monitoring the subsequent evolution using a delayed pulse (the "probe"), TAS can provide valuable insights into transient electronic states, charge carriers dynamics, energy transfer processes, vibrational modes, and reaction intermediates. This technique has been extensively applied in various fields to characterize photovoltaic materials, photochemical reactions, and biological systems.[36–38] However, there are very few examples of its use for the study of electrocatalysts.

Herein, we synthesize a series of M–N–C catalysts incorporating Fe and Co transition metal centers on N- and P-doped carbon. We employ TAS to elucidate the doping effect of p-block and metal incorporation on the electronic structure of the materials. We thus offer unprecedented insight of the charge-trapping sites in M–N–C electrocatalysts for ORR. Additionally, density functional theory calculations were also performed to calculate isosurface charge density difference (CDD) and integrated charge density (ICD) to gain a deeper understanding of the material's electronic properties and its influence on ORR activity. Our findings corroborate existing theories and reveal new insights into the fundamental processes governing catalytic efficiency.

Experimental

Material synthesis

Synthesis of polymeric precursors. Polyaniline (PANi) hydrogels were synthesized *via* oxidative polymerization of aniline monomers in the presence of phytic acid at room temperature in aqueous solution. To achieve this, aniline (Sigma Aldrich) and phytic acid (Sigma Aldrich) were mixed in volume ratios of 1 : 1 to 1 : 4, while maintaining a total volume of 20 ml. In a separate container, 1.96 g of ammonium persulfate (Sigma Aldrich) was dissolved in 10 ml of deionized (DI) water. Both solutions were cooled to 4 °C in a refrigerator before being combined and then left unstirred at room temperature for 1 hour to form a hydrogel. The resulting hydrogels were then immersed in a beaker containing 2 L of DI water for 48 hours. Stable, self-supporting hydrogels were only observed for an aniline to phytic acid ratio of 1 : 4, but the products resulting from other ratios were nevertheless collected for further analysis. The polymerization products were subsequently washed with ~3 L of DI water by vacuum filtration through a nylon membrane filter with a 0.2 μm pore size. Finally, the obtained polymers were placed in a freeze-dryer (Labogene ScanVac CoolSafe, 4L Basic Freeze Dryer, Denmark) at −55 °C for 24 h to form aerogels, which took the form of a dark green powdery product.

Pyrolysis conditions. The obtained powders were then pyrolyzed in a tube furnace (AS ONE) at 1000 °C for 2 h, using a heating rate of 5 °C min^{-1}, under flowing nitrogen (100 ml min^{-1}). The resulting samples are herein referred to as N/P-C-1, N/P-C-2, N/P-C-3, and N/P-C-4, where N, P and C refer to nitrogen, phosphorus and carbon, respectively. The numbers correspond to the ratio of phytic acid to aniline in the precursor polymer. Pyrolysis of N/P-C-4 resulted in the formation of a fine black powder, whilst the remaining three samples formed dense agglomerated powders that required crushing in a mortar and pestle before further analysis.

Iron and cobalt decoration. 100 mg of N/P-C-4 was dispersed in 50 ml of DI water, whilst 10.2 mg of either iron phthalocyanine (Tokyo Chemical Industry Co. Ltd) or 9.7 mg of cobalt phthalocyanine (Tokyo Chemical Industry Co. Ltd) were ultrasonically dispersed in 10 ml of DI water (corresponding to an iron or cobalt loading of 1 wt%). The N/P-C-4 and metal phthalocyanine mixtures were then combined and sonicated for 30 minutes before being dried on a hot plate until all the solvent was completely evaporated. Subsequently, the samples were subjected to a second pyrolysis step at 900 °C for 2 hours with a heating rate of 5 °C min^{-1}, under nitrogen flow (100 ml min^{-1}). The pyrolysis products were then washed with 1 M H_2SO_4 (Wako, Japan) followed by vacuum filtration to remove

unreacted metal salts or exposed crystalline metallic phases. The resulting samples are labeled as Fe–N/P-C-4 and Co–N/P-C-4, respectively.

Physical characterization

Powder X-ray diffraction (XRD) patterns were collected on a silicon wafer with a Bruker-AXS D8 diffractometer using Cu Kα (λ = 1.5418 Å) radiation and a LynxEye position sensitive detector in Bragg Brentano parafocussing geometry, from 10 to 50°. The samples were pressed on the silicon wafer with a glass slide for homogeneity. Scanning electron microscopy (SEM, Hitachi S-5200, HD-2300A) and cold field emission gun high-resolution analytical transmission electron microscopy (TEM, JEOL F200 80–200 kV) were used to determine the morphology of the synthesized samples. The specific surface area was calculated using the Brunauer–Emmett–Teller (BET) nitrogen adsorption–desorption method (BELSORP-mini, BEL Japan, Inc.). X-ray photoelectron spectroscopy (XPS) was performed using a Kratos Supra instrument with a monochromated aluminium source. Chemical and local atomic bonding analysis was also performed by electron energy loss spectroscopy (EELS). UV-vis absorption measurements were taken using an Agilent Cary 60 UV-vis spectrometer.

TAS UV-vis pump–probe spectroscopy experiments were performed in the Lord Porter Ultrafast Laser Laboratory at the University of Sheffield, using a commercial Helios system (HE-VIS-NIR-3200, Ultrafast Systems). Narrowband pump pulses at 267 nm were generated using a TOPAS Prime optical parametric amplifier (Spectra Physics), which has a tunable output range of 290–1600 nm. The generated pulses had an output power of 1 mW. The TAS module was seeded by a regenerative amplifier (Spitfire ACE PA-40, Spectra-Physics), which provided 800 nm pulses (40 fs FWHM, 10 kHz, 1.2 mJ). The pump was focused onto the sample suspension at a beam diameter of approximately 275 μm. The white-light probe continuum (~440 to 700 nm) was generated using a portion of the amplifier fundamental focused onto a sapphire crystal. The probe light, after passing through the sample, was collected using a spectrometer and a complementary metal oxide semiconductor (CMOS) camera, with a resolution of 1.5 nm. The timing between pump and probe pulses is set *via* a computer-controlled optical delay line (DDS300, Thorlabs), which provides up to 8 ns of pump–probe delay. The pump and probe pulses were set to a relative polarization of 54.7° for the measurements, corresponding to the magic angle. The instrument response function was approximated to be 100 fs, based on the temporal duration of the coherent artifact signal from the quartz substrate. The acquisition and preprocessing of the pump–probe data were performed using Surface Xplorer provided by Ultrafast Systems. The samples were ultrasonically dispersed in ethanol prior to measurement. Ethanol was used as a non-interactive solvent. All TAS measurements were conducted in a 1 mm pathlength quartz cuvette, with steady-state absorption kept at ~0.5 OD.

Terahertz spectral measurements were performed on an instrument that has been described elsewhere.[39] In brief, the system used a mode-locked Ti:sapphire laser (Vitara, Coherent) providing pulses with a width of 20 fs at an 80 MHz repetition rate centered at 800 nm. The beam was split into two, and the higher power beam (~400 mW) was sent through a mechanical delay before being used to excite the THz emitter. Meanwhile, the lower power beam (~100 mW) was used for detection. Both emitter and detector comprise low-temperature grown gallium arsenide (LT-GaAs) on quartz substrates (LoQ) photoconductive (PC) devices with a large-area slot electrode design with a 4 mm-long gap. The emitter has a 200 μm-wide gap, while the detector used has a 100 μm-wide gap and the emitter was electrically biased with a modulation frequency of 1 kHz, with a 50% duty cycle, to enable lock-in detection while the current generated detector was amplified using a *trans*-impedance amplifier with a gain of 1×10^8 Ω.

Once THz radiation is generated by excitation of the emitter, it is collected by a pair of off-axis parabolic mirrors, focused onto the sample before being recollected by a second set of off-axis parabolic mirrors and focused onto the PC detector along with the weaker optical beam. Detection is performed by varying the delay between the two arms and recording the current using a lock-in amplifier (10 ms time constant), referenced to the emitter bias-modulation frequency.

To prepare a sample for THz measurements, the catalyst powder was mixed with polytetrafluoroethylene powder (PTFE, 1 μm particle size, Sigma Aldrich) with a mass ratio of 1 wt%. 40 mg of the mixed powder was then pressed using a Specac manual hydraulic press and a 13 mm die with 8 tons of pressure for approximately 10 minutes. The die also included a copper washer ~400 μm thick that surrounds the pressed pellet and provides rigidity for the spectral measurements. A reference was recorded without the sample present, before a second measurement was performed with the sample in the focus of the THz beam. These measurements were then compared to determine the spectral properties of these pellets.[40]

Electrochemical characterization

Electrochemical measurements were performed according to guidelines recommended by the Fuel Cell Commercialization Conference of Japan (FCCJ).[41] The ORR performance was determined using a three-electrode rotating ring disk electrode (RRDE) setup in either 0.1 M potassium hydroxide (KOH, Wako, Japan) or 0.1 M perchloric acid ($HClO_4$) electrolyte solution. The reference electrode was Ag/AgCl in saturated KCl, and the counter electrode was a platinum wire. Potentials are quoted relative to the reversible hydrogen electrode (RHE).[42] The glassy carbon working electrode (0.196 cm^2, Hokuto Denko Corporation) was polished and then cleaned by ultrasonication in DI water for 15 minutes. Electrocatalyst ink was prepared by dispersing 4 mg of non-PGM catalyst in a mixture of DI water, 5 wt% Nafion solution (in a mixture of lower aliphatic alcohols and water), and ethanol in a 3 : 1 : 3 ratio by volume, followed by sonication for at least 30 minutes. An 8 μl drop of the catalyst ink was then carefully deposited onto the working electrode and dried in air at 60 °C for 15 minutes, corresponding to a catalyst loading of 580 μg cm^{-2}. A commercial 46.1 wt% platinum-decorated (Tanaka Kikinzoku Kogyo Corp., Japan) carbon black catalyst was also investigated for comparison, dispersed in a mixture of DI water, ethanol and

5 wt% Nafion solution in a ratio of 19 : 6 : 0.1. A 10 μl droplet of the dispersion was applied to the working electrode, corresponding to a loading of 17.3 μg cm^{-2}.

An automatic polarization system, a rotating ring-disk electrode setup, and a three-electrode electrochemical cell (models HZ-5000, HR-500, and HX-107, respectively, Hokuto Denko Corp.) were used. Cyclic voltammograms (CV) were recorded in nitrogen gas saturated electrolytes in the range 1.17 to −0.03 V_{RHE} at a scan rate of 50 mV s^{-1}. Linear sweep voltammograms (LSVs) were measured in oxygen gas-saturated electrolyte at scan rates of 10 mV s^{-1} at 400, 900, 1600 and 2500 rotations per minute (rpm). Electrolytes were saturated by bubbling each respective gas through the solution for 30 minutes before each experiment, and a continuous flow was then maintained throughout the measurement. All the LSVs are presented after subtracting the blank current measured in the nitrogen-saturated electrolyte from the current measured in the oxygen-saturated electrolyte.

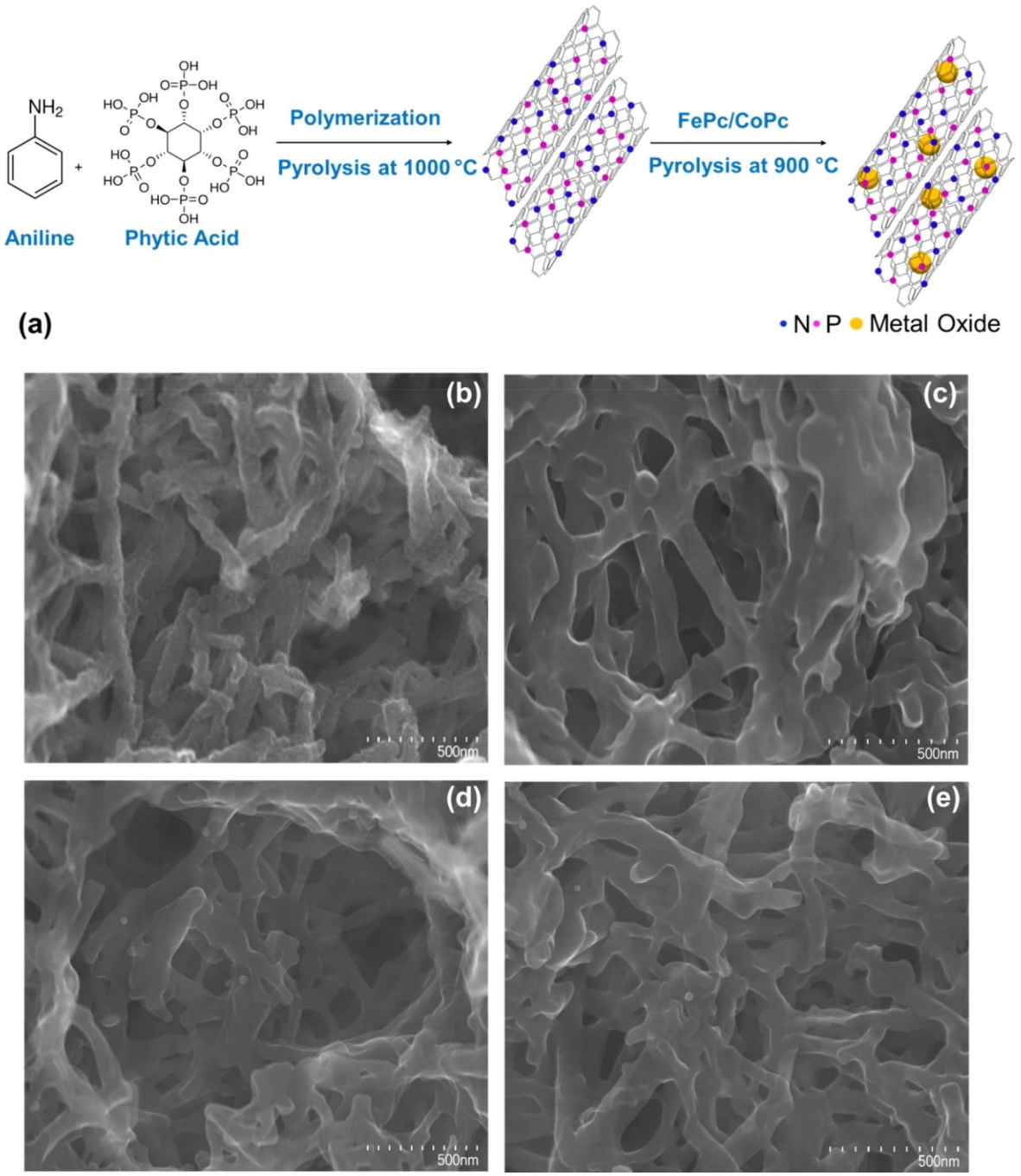

Fig. 1 (a) Schematic illustration of the two-step synthesis of metal-decorated nitrogen- and phosphorus-doped carbon fibers. (b) SEM image of the phosphorus-doped PANi aerogel (1 : 4 ratio of aniline to phytic acid), before pyrolysis. (c) SEM image of the metal-free N/P-C-4 electrocatalyst after pyrolysis at 1000 °C. (d and e) SEM images of metal-decorated electrocatalysts Co–N/P-C-4 and Fe–N/P-C-4, respectively.

Results

Material characterization

The obtained catalysts were fine black powders. The mass yield after the first pyrolysis of the PANi aerogel was 23%, while the overall yield after metal decoration and acid washing was around 6%. N/P-C-4, prepared with a 1 : 4 ratio of aniline to phytic acid, was the only sample to form a clear aerogel-type structure. Fig. 1 shows the morphology of the N/P-C-4 sample before and after pyrolysis, obtained *via* SEM. Before the polymerization pyrolysis (Fig. 1b), the aerogel already displays a clear three-dimensional fibrous morphology with a fiber diameter of <100 nm. The surface of the fibers appears to be slightly rough, which may be attributed to the presence of unreacted aniline and phytic acid. After the pyrolysis (Fig. 1c), the three-dimensional network and the fiber dimensions are retained; however, the individual fibers are more interconnected, and the surface is much smoother. This slight difference in morphology is attributed to partial melting of the structure during pyrolysis. After decoration with cobalt (Fig. 1d) or iron (Fig. 1e and S4a†) *via* a second pyrolysis step, no further significant changes in morphology are observed, and no metal particles are observed to within the resolution limit of the SEM.

Fig. S2† demonstrates that samples prepared using different phytic acid to aniline ratios resulted in much denser carbons without a fibrous microstructure, as discussed subsequently. This is attributed to the fact that phytic acid acts both as a dopant and surfactant, with the surfactant properties playing an important role in the formation of a stable hydrogel and subsequent retention of that morphology as an aerogel.[28]

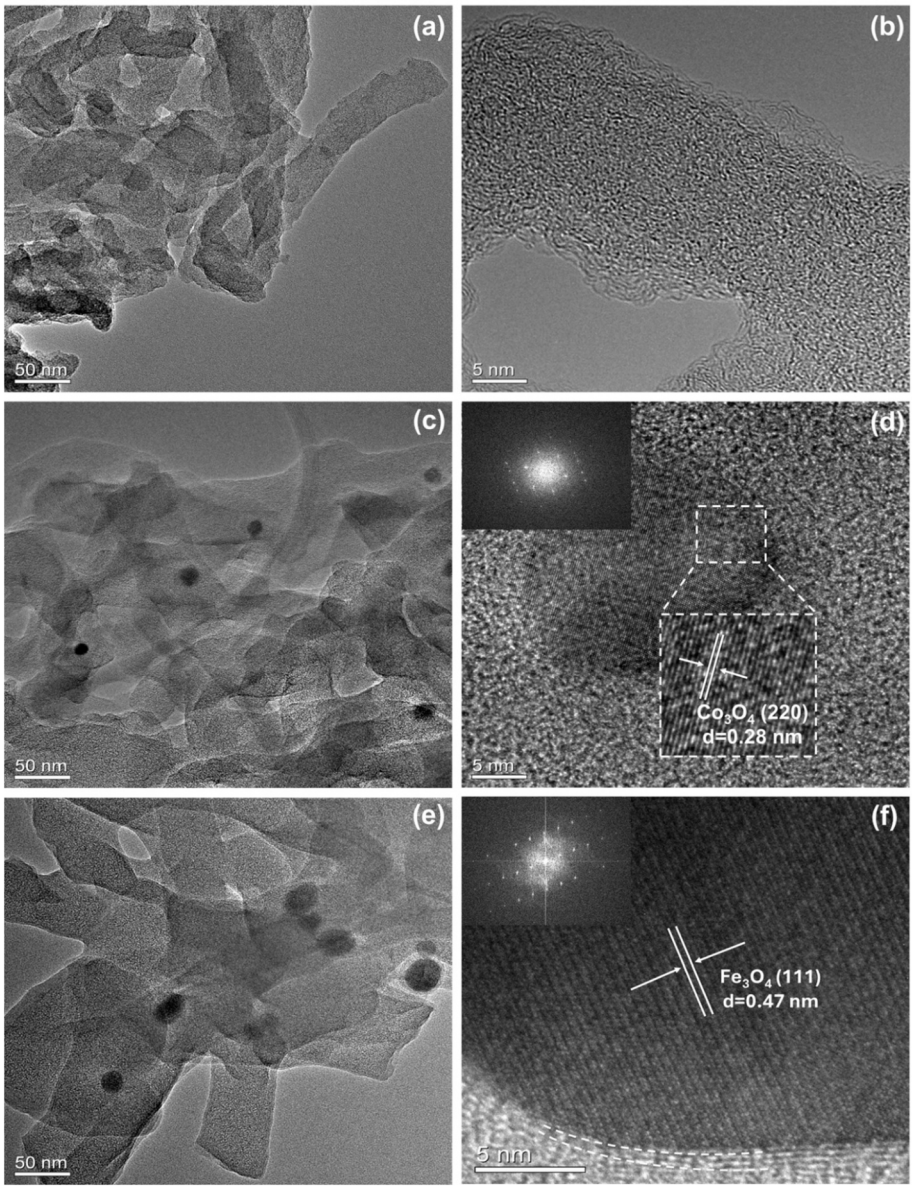

Fig. 2 HR-TEM images of the synthesized materials: (a and b) N/P-C-4; (c and d) Co–N/P-C-4 with FFT of an individual nanoparticle (inset); (e and f) Fe–N/P-C-4 with FFT of an individual nanoparticle (inset).

Additionally, the material was pyrolyzed at 1100 °C, and the corresponding SEM image is shown in Fig. S3.† However, in this case melted microstructures were observed instead of distinct fibers, likely due to thermal decomposition and instability of the precursors at this temperature which is consistent with previous studies.[43]

HR-TEM was employed to further investigate the microstructure and morphology of the samples at higher magnification. The fibrous structure of N/P-C-4 is confirmed, and the approximate diameter is about several tens of nanometers (Fig. 2a). Higher magnification (Fig. 2b) reveals that the fibers do not have significant graphitic phases and have the appearance of turbostratic or completely amorphous carbon. After metal decoration, the microstructure does not significantly change, but several nanoparticles are observed in dark contrast for both Co–N/P-C-4 (Fig. 2c) and Fe–N/P-C-4 (Fig. 2e and S4b†). HR-TEM images and their corresponding fast Fourier transforms (FFT) confirm that these nanoparticles are primarily comprised of Co_3O_4 (Fig. 2d) and Fe_3O_4 (Fig. 2f).

The nature of the nanoparticle observed in Fig. 2e (Fe–N/P-C-4) was also confirmed by EELS (Fig. 3c). The combination of the Fe L-edge at ~700 eV (corresponding to Fe^{2+} and Fe^{3+} oxidation states) and the oxygen K-edge at ~530 eV further corroborates the existence of magnetite (Fe_3O_4) in which iron exists in both +2 and +3 oxidation states.[44]

Since these metal oxide particles were not removed during the acid washing step, it is likely that they are encapsulated by a thin layer of graphitic carbon, a three to four layers example of which is visible in Fig. 2f and S4c.† Such structures are commonly observed in the literature.[45,46] It should also be noted that catalytic activity in M–N–C electrocatalysts is generally attributed to the presence of atomically dispersed metallic sites such as $Co_{2/4}$-N or $Fe_{2/4}$-N. These are not readily observable in conventional HR-TEM observation, but it is likely that they co-exist with the metal oxide nanoparticles observed in these samples.

XRD was used to investigate the crystal structure of the unpyrolyzed PANi samples synthesized with different aniline to phytic acid ratios (Fig. 3a). PANi generally displays three major characteristic peaks at ~15°, 20° and 25°, associated with the (011), (020) and (200) crystal planes. The (011) plane corresponds to the periodicity associated with the amorphous regions and interchain distances perpendicular to the polymer backbone; the (020) plane to the periodic arrangement of PANi chains and the interchain separation due to π–π stacking interactions; and the (200) plane to π–π stacking of the aromatic rings within the ordered domains of the polymer chains. These characteristic peaks were observed for all phytic acid ratios. However, as the proportion of phytic acid increases, the diffraction profile changes dramatically. For the 1 : 4 ratio, the peaks are very broad, suggesting a more amorphous structure. This could correspond to the fully doped form of PANi, emeraldine salt (ES). The 1 : 3 and 1 : 2 ratios display sharper peaks, potentially corresponding to the partially doped

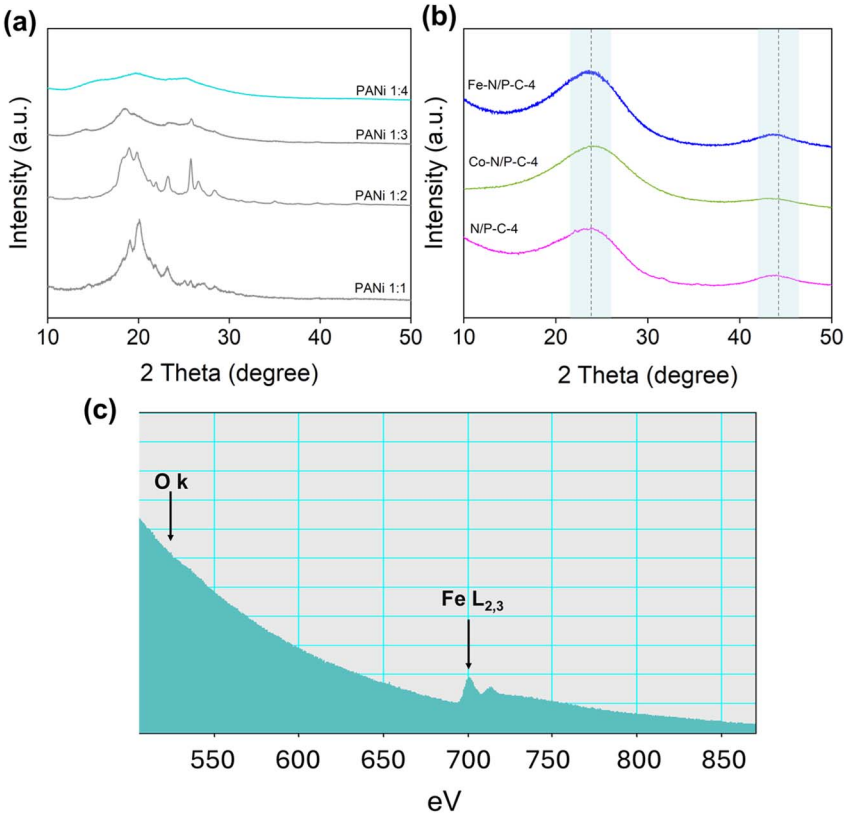

Fig. 3 (a) XRD pattern of PANi aerogels synthesized by mixing different ratios of phytic acid and aniline. (b) X-ray diffraction patterns of N/P-C-4, Co–N/P-C-4 and Fe–N/P-C-4 (c) electron energy-loss spectrum (EELS) of a single nanoparticle with the oxygen K and Fe L 2,3 edges indicated.

emeraldine salt form of PANi. The 1 : 1 ratio displays the sharpest peaks, which correspond closely to the profile of the undoped emeraldine base (EB) form of PANi. This is in agreement with the increasing degree of oxidation expected as the amount of phytic acid increases.[47–49]

After pyrolysis of the PANi precursors at 1000 °C, the three characteristic diffraction peaks of PANi are no longer visible in all samples, indicating a significant transformation in the crystal structure as the samples transition from a polymeric to a carbonaceous state (Fig. 3b and S1†). This confirms that the observed diffraction peaks at ~24° and ~44° are characteristic of the (002) and (101) crystal planes of carbon, respectively.[50,51] The peaks are relatively broad, suggesting that the resulting carbon material is turbostratic or amorphous rather than graphitic. After metal decoration, there is no significant change in the XRD profiles (Fig. 3b). This indicates that decorating with Fe or Co does not significantly alter the structure of the underlying carbon. No peaks corresponding to metallic or oxide forms of iron or cobalt are present (despite clearly being observed in the HR-TEM images). This is likely due to the very low metal loading resulting in weak diffraction.

The textural characteristics of the PANi polymers prepared with different aniline to phytic acid ratios were determined from nitrogen gas adsorption isotherms. The resulting BET surface areas were 4, 12, 23, and 56 $m^2\ g^{-1}$ for ratios of 1 : 1, 1 : 2, 1 : 3, and 1 : 4, respectively (Fig. S5a and b†). These relatively low values are typical for PANi type polymeric materials.[52] However, it is also evident that changing the precursor ratios does have a clear effect on the microstructure (in agreement with the SEM images), with the fibrous aerogel structure formation from the 1 : 4 ratio resulting in increased surface area, as expected. After pyrolysis of the respective PANi polymers, the surface areas increased to 5, 79, 96 and 435 $m^2\ g^{-1}$, respectively (Fig. S5c and d†). The optimized phytic acid to aniline ratio clearly leads to a significantly larger surface area, and pore volume (0.4 $cm^3\ g^{-1}$). This is attributed to the fibrous morphology of the aerogel in that case but also hints that phytic acid can act as a pore-forming or activation agent during carbonization. Indeed, phytic acid is a well-known activation agent.[53,54]

The impact of the subsequent metal decoration step on the surface area and porosity was also investigated. We observed another significant increase in surface area to 801 $m^2\ g^{-1}$ for the Co-decorated sample and 817 $m^2\ g^{-1}$ for the Fe-decorated sample (Fig. 4a). Meanwhile, the pore volumes also increase to 1.0 and 1.3 $cm^3\ g^{-1}$, for Co- and Fe-decorated samples, respectively. These increases are attributed to a combination of conventional gasification during the additional pyrolysis step, as well as metal-catalysed gasification of the carbon support. This is in agreement with the pore size distribution (Fig. 4b), which shows a clear increase in the frequency of pores with large diameters of ~50 to 150 nm. This is also in clear agreement with the observed mass loss (*i.e.* decreased yield) during the metal-decoration step. Type IV isotherms were observed for N/P-C-4, Co–N/P-C-4 and Fe–N/P-C-4 samples. The Type IV isotherms are characteristic of a combination of mesoporous and microporous structures.[55] Additionally, the pore volumes and surface area values for all the samples are given in Table S1,† and surface areas are also directly compared in Fig. 4c.

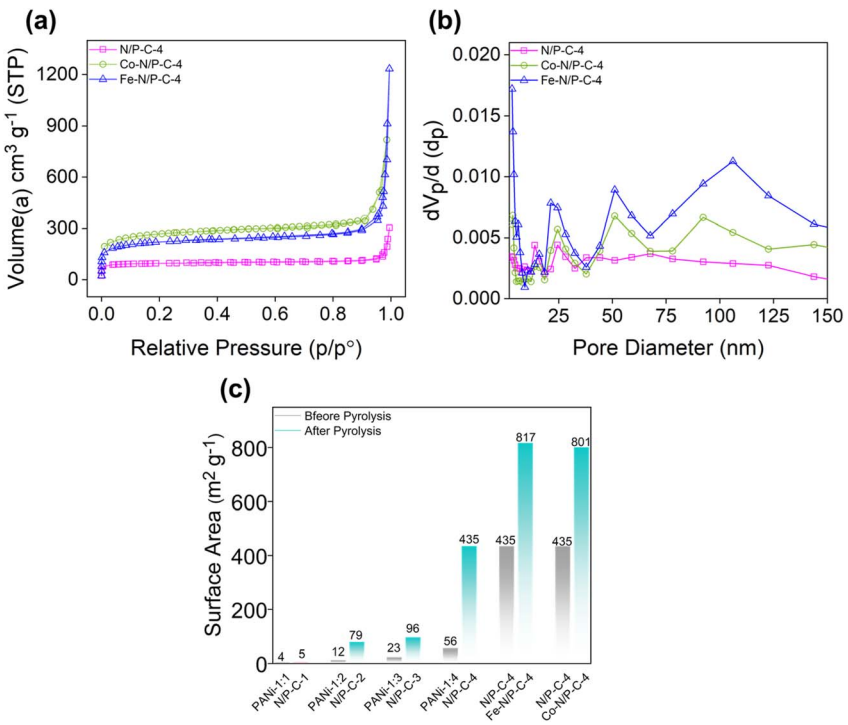

Fig. 4 (a) BET Isotherm, and (b) pore distribution of N/P-C-4, Co–N/P-C-4 and Fe–N/P-C-4. (c) Bar graph comparing the surface area before and after pyrolysis and after metal decoration for all samples.

XPS was used to confirm the chemical states of different elements present in the samples. Elemental analysis *via* survey scans (Fig. S6†) confirms the presence of carbon (~284.5 eV), nitrogen (~400.0 eV), phosphorus (~133.3 eV), and oxygen (~532.0 eV) in all samples, as well as iron (~711.0 and ~725.0 eV) and cobalt (~781.6 eV and 797.2 eV) in the corresponding metal-decorated samples. This confirms the successful doping of carbon with nitrogen and phosphorus, as well as decoration with metal.

The phytic acid doped PANi precursor (1 : 4) contained ~9.7 at% nitrogen (from PANi), 3.8 at% phosphorus (from the phytic acid) and 12.2 at% oxygen (also mainly attributed to the phytic acid). After pyrolysis, these values fall to 3.1, 2.0, and 5.5 at%, respectively, highlighting the changes in surface chemistry during the thermal treatment. The decrease in phosphorus and oxygen contents is likely attributed to the loss of phosphate groups during pyrolysis. After metal decoration with Co and Fe, the nitrogen content does not change significantly (possibly due to the additional nitrogen atoms in the metal phthalocyanine molecules); the phosphorus content slightly decreases (to 1.6 and 1.9 at% in Co- and Fe-decorated samples respectively); and the oxygen content slightly increases as expected for the high surface area carbon materials due to the increased porosity.[56] The resulting cobalt and iron concentrations are ~0.6 and ~0.7 at% according to these results. Detailed elemental compositions of all the samples are summarized in Table S3.†

High-resolution XPS scans reveal more detailed information about the chemical states of each element present in the samples. For the phytic acid doped PANi precursor (Fig. S7a†) the C 1s spectra was deconvoluted into four peaks: C=C/C–C at 284.6 eV (attributed to the backbone of PANi); C–N at 285.8 eV (attributed to the amino group in PANi), C–O at 287.7 eV (attributed to hydroquinone in phytic acid); and a π–π* transition at ~291.0 eV.[57] After pyrolysis and metal decoration, the C 1s spectra of N/P-C-4, Co–N/P-C-4 and Fe–N/P-C-4 are all similar: C=C at 284.4 eV (characteristic of sp^2 carbon), C–P/C–O at 285.6 eV (attributed to phosphorus doping), C–N/C–C at 285 eV (attributed to nitrogen doping), and a carbon π–π* transition at ~290 eV (Fig. S7b–d†).

The P 2p region for the phytic acid doped PANi aerogel (Fig. S8a†) reveals a signal with a Gaussian-type distribution

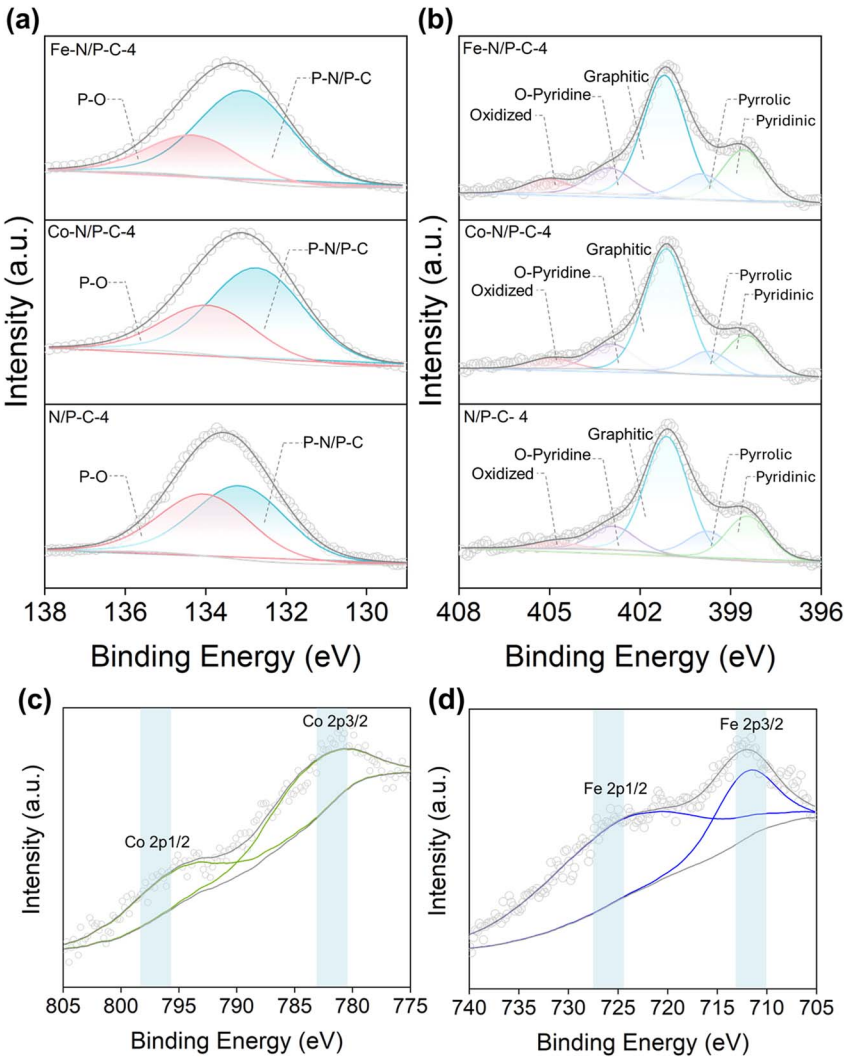

Fig. 5 X-ray photoelectron spectroscopy: (a) P 1s and (b) N 1s regions of N/P-C-4, Co–N/P-C-4 and Fe–N/P-C-4. (c) Co 2p region for Co–N/P-C-4 and (d) Fe 2p region for Fe–N/P-C-4.

centered at ~133 eV. This is attributed directly to the phosphorus atoms in phytic acid (P–O/P═O).[58,59] After pyrolysis, the signal still has a Gaussian profile, but the center is slightly shifted to 133.5 eV (Fig. 5a). This reflects the decrease in the contribution from the P–O groups of phytic acid (at ~135 eV), and an increase in the proportion of phosphorus doped into the carbon network (P–C at 131.8 eV; P–N at 133 eV; and P–O at 135 eV).[43,60] Furthermore, after metal decoration, no significant change is observed in the P2p region.

The N 1s region of the phytic acid doped PANi aerogel (Fig. S8b†) has a signal with a Gaussian profile centered at approximately 400 eV. This is expected to correspond to the C–N–C environment in the molecular structure of PANi. Meanwhile, after pyrolysis, the N 1s region of all the heat-treated samples is typical of pyrolyzed nitrogen-doped carbon materials and can be roughly deconvoluted into pyridinic (398 eV), pyrrolic (399 eV), graphitic (401 eV), O-pyridine (402.7 eV), and oxidized pyridinic (403.5 eV) contributions.[61] Furthermore, the profiles of the N 1s regions do not change significantly after the metal-decoration step, even around 399 to 400 eV, where Fe–N or Co–N contributions would typically appear. The relative percentages of deconvoluted nitrogen for all samples are summarized in Table S3.†[62]

Finally, small signals corresponding to iron and cobalt are observed but these signals are too small for meaningful deconvolution (Fig. 5c and d). Peaks at ~711 and ~725 eV are attributed to Fe^{3+} and Fe^{2+} species in the Fe 2p 3/2 and Fe 2p 1/2 regions for Fe–N/P-C-4, whilst peaks at ~782 and ~797 eV are attributed to Co^{3+} and Co^{2+} species in the Co 2p 3/2 and Co 2p 1/2 regions for Co–N/P-C-4 samples. This likely indicates the presence of Fe_3O_4 and Co_3O_4 species alongside Fe–N and Co–N moieties.[63–65]

Terahertz spectral analysis was performed on PTFE pellets mixed with N/P-C-4, Co–N/P-C-4 and Fe–N/P-C-4 (1 wt%) to assess the dielectric properties and the impact of transition metal doping on the charge transport and structural order in the material. The real permittivity (material's ability to store electrical energy) of the three pellets is shown in Fig. 6a, whilst the imaginary permittivity (corresponding to energy dissipation within the material) is displayed in Fig. 6b. The real permittivity shows a clear sensitivity to transition metal decoration, with Fe–N/P-C-4 showing lower permittivity compared to Co–N/P-C-4 across the frequency range measured. This may explain the superior electrocatalytic performance demonstrated by this material, as it shows the presence of distinct active sites in the material. Meanwhile, no clear trend is observed in the imaginary permittivity.

Electrochemical characterization

First, the electrochemical performance of the pyrolyzed samples prepared using different ratios of aniline to phytic acid was measured in 0.1 M KOH solution. Fig. 7a shows that N/P-C-1, N/P-C-2, and N/P-C-3 have similar onset potentials and relatively low diffusion-limited current densities. Meanwhile, N/P-C-4 has a much larger diffusion-limited current density, which is attributed to the much higher surface area. Next, the N/P-C-4 is compared directly with the metal decorated samples (Fig. 7b). The metal-free sample has the lowest onset potential of around 0.88 V *vs.* RHE, with Co–N/P-C-4 displaying a slightly higher onset potential (around 0.90 V *vs.* RHE), and Fe–N/P-C-4 displaying the highest onset potential (0.93 V *vs.* RHE). Meanwhile, the corresponding half-wave potentials are 0.73, 0.76 and 0.84 V *vs.* RHE, respectively. The results were also compared against a Pt/C catalyst, which displays similar onset potential to that of Fe–N/P-C-4, but with significantly lower limiting current density (platinum is not generally more active compared to M–N–C electrocatalysts in alkaline media). These trends clearly highlight the superior ORR activity of the metal-decorated samples in alkaline conditions, especially the iron-decorated catalysts.

Furthermore, Tafel slopes were calculated to gain insights into the reaction kinetics of the synthesized electrocatalysts (Fig. 7c). The Tafel slope is crucial for identifying rate-determining step (RDS) in electrocatalytic processes. A slope of approximately 60 mV dec^{-1} suggests faster kinetics with electron transfer as the RDS, while a slope of around 120 mV dec^{-1} indicates slower kinetics, often attributed to intermediate H_2O_2 formation. The Tafel slopes of N/P-C-4, Co–N/P-C-4, Fe–N/

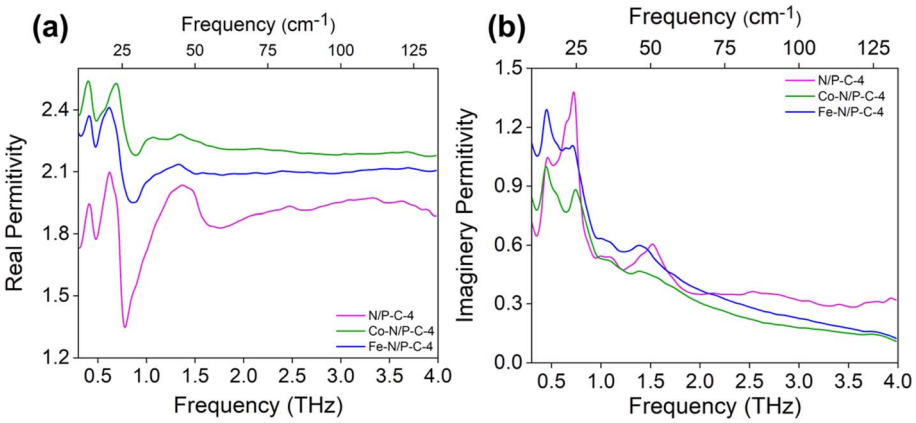

Fig. 6 (a) Real and (b) imaginary THz permittivity of N/P-C-4, Co–N/P-C-4 and Fe–N/P-C-4 mixed with PTFE binder (1% w/w) and pressed into pellets.

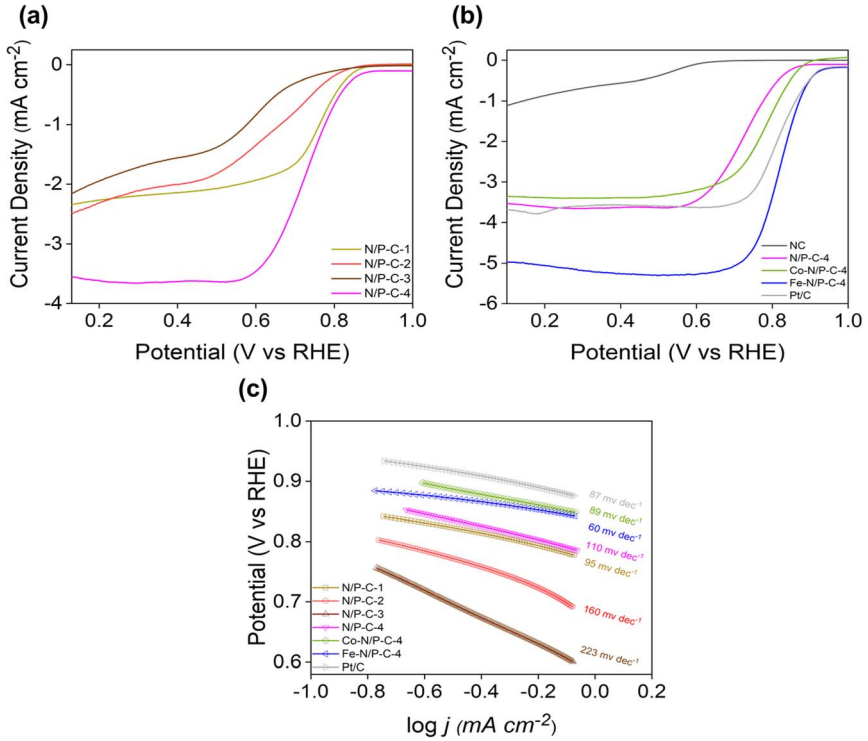

Fig. 7 ORR activity measured at 1600 rpm in 0.1 M KOH: (a) LSVs of metal-free catalysts with different phytic acid ratios; (b) LSVs comparing metal-free and metal-decorated electrocatalysts; (c) comparison of the Tafel slopes of all synthesized electrocatalysts.

P-C-4 and Pt/C are calculated to be 110, 89, 60 and 87 mV dec^{-1}, respectively. The Tafel slope values were also calculated for samples synthesized using other phytic acid-to-aniline ratios. For N/P-C-1, N/P-C-2, and N/P-C-3, the values were 95 mV dec^{-1}, 160 mV dec^{-1}, and 223 mV dec^{-1}, respectively. These results suggest that the metal-free samples have the slowest kinetics towards the ORR, as expected. However, N/P-C-1 has a better Tafel slope than N/P-C-2 and N/P-C-3, which can be attributed to higher nitrogen content determined by XPS (in turn due to the higher proportion of aniline used in the synthesis of this sample). This is followed by the cobalt-decorated sample and Pt/C, which have similar Tafel slopes. Finally, the iron-decorated sample has the fastest kinetics in the alkaline medium.

CV plots and polarization curves for the three electrocatalysts obtained at different rotation speeds are shown in Fig. S9(a–c).† Corresponding K–L plots are shown in the inset, from which the electron transfer number (n) was determined to be 3.5, 3.7, and 3.9 for N/P-C-4, Co–N/P-C-4, and Fe–N/P-C-4, respectively. Pt/C also has an n value of ~3.9. This confirms that Fe–N/P-C-4 has the highest selectivity towards the 4-electron ORR pathway, in reasonable agreement with the Tafel slope. The long-term stability was evaluated using chronoamperometry, which demonstrated that the catalyst retained approximately 94% of its initial current after ~10 hours of operation (Fig. S10†).

Meanwhile, the ORR was also investigated under acidic conditions in 0.1 M $HClO_4$ electrolyte. A similar trend in ORR activity was observed compared to KOH electrolyte, with onset potentials of 0.74, 0.84, 0.86 V and 0.93 V *vs.* RHE for N/P-C-4, Co–N/P-C-4, Fe–N/P-C-4, and Pt/C, respectively (Fig. 8a). Similarly, the half-wave potentials are 0.67, 0.51, 0.69 and 0.81 V *vs.* RHE, respectively. The Tafel slopes (Fig. 8b) for N/P-C-4, Co–N/P-C-4, Fe–N/P-C-4 and Pt/C are calculated to be 116, 74, 78 and 69 mV dec^{-1}, respectively. These results indicate that the metal-free sample exhibits the slowest kinetics towards the ORR in acidic media (as expected), followed by the cobalt-decorated sample and then the iron-decorated sample. Pt/C exhibits the fastest kinetics in acidic media, as expected. Overall, in this case, the iron-decorated sample shows the highest ORR activity among M–N–Cs. Furthermore, the measured values are lower than those obtained in alkaline conditions due to the slower kinetics in acidic media. The CV curves of N/P-C-4, Co–N/P-C-4 and Fe–N/P-C-4 in nitrogen and O_2 saturated electrolytes and polarization curves for the three electrocatalysts obtained at different rotation speeds in 0.1 M $HClO_4$ are shown in Fig. S11(a–c).† The K–L plots are shown in the corresponding insets, from which the electron transfer number (n) was determined to be ~3.9 for Fe–N/P-C-4. CV plots in N_2 saturated electrolyte do not show any faradaic peak, indicating no chemical activity. However, in O_2 saturated, the peak is evident. The peak is more positive in Fe–N/P-C-4 compared to Co decorated and metal-free samples, showing faster kinetics.

Overall, the metal-decorated samples display significantly improved ORR activity in both acidic and alkaline media compared with the metal-free support. This confirms the impact of introducing metal-active sites alongside P and N in the carbon network. Comparing the two transition metal dopants, Fe–N/P-C-4 displays significantly enhanced activity in

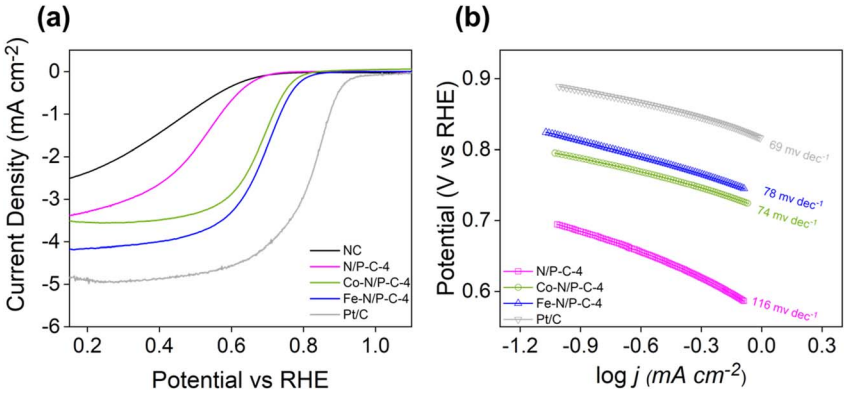

Fig. 8 ORR activity measured at 1600 rpm in 0.1 M $HClO_4$: (a) LSVs comparing metal-free and metal-decorated electrocatalysts; (b) comparison of the corresponding Tafel slopes.

both alkaline and acidic media. Moreover, the electrochemical activity directly corresponds to the isosurface charge density difference (CDD) and integrated charge density (ICD) calculations. The CDD and ICD were measured to visualize and quantify charge redistribution in N/P-C-4, Co–N/P-C-4 and Fe–N/P-C-4 samples (Fig. S12 and S13†). The calculations highlight that transition metal doping significantly affects charge redistribution. These changes provide direct insights into electron transfer efficiency and active site formation, allowing for a predictive understanding of ORR activity. A detailed discussion is provided in the ESI.†

Transient state absorption spectroscopy

Herein, we employ time-resolved TAS as a novel method to probe the ultrafast electronic properties of the pyrolyzed metal-free and metal-decorated samples to gain new insights into properties related to their activity towards the ORR. For the analysis, a femtosecond transient absorption pump–probe setup was used. The sample is excited by the pump pulse, and the probe pulse is used to monitor the transient local electronic properties of the material *via* the monitored differential absorption spectrum (ΔA). The delay time between the pump and probe pulses is precisely controlled to obtain time-resolved information.

Before TAS, steady-state UV-visible (Fig. S14†) absorption was performed to identify the characteristic absorption wavelength for TAS. A broad peak centered at 267 nm was observed among all three samples (N/P-C-4, Co–N/P-C-4 and Fe–N/P-C-4). This is attributed to the $\pi \rightarrow \pi^*$ transition, which is characteristic of graphitized carbon materials. Therefore, a wavelength of 267 nm was selected for the exciting pump pulse in TAS measurements.[66,67]

Fig. 9a–c shows the resulting kinetic traces with multi-exponential fittings. These correspond to the time-dependent evolution of the change in optical absorption (ΔA) at a delay time (t) after the excitation pulse, at a specific probe wavelength, 400 nm in this case, as it exhibits significant absorption and strong transient signals. Positive values indicate excited state absorption (ESA), while negative values suggest ground-state bleaching (GSB) or stimulated emission (SE).

The data are represented into three separate graphs for each sample. The first shows the early kinetics up to 2 ps, the second covers 2 to 500 ps, and the third spans from 500 ps to 6 ns. During excitation around $t = 0$, the ΔA signal rapidly increases to a maximum positive value within femtoseconds, reflecting the initial population of excited states. The signal then decays back to near zero over a few hundred femtoseconds. Given that the 267 nm pump induces a $\pi \rightarrow \pi^*$ transition, the initial excitation primarily generates delocalized excitons or hot carriers, which subsequently relax through carrier–carrier scattering, or other non-radiative pathways reflecting relaxation of the excited state population and the return of the system toward its equilibrium state.[68]

For the metal-free sample (N/P-C-4) the ΔA signal (Fig. 9a) transitions to a very small but persistent negative ΔA value after ~250 ps. The graph reveals three distinct time components: an initial fast decay with a lifetime of (~73 fs) attributed to band gap renormalization caused by photogenerated hot carriers heating the lattice. This was followed by a slower decay with a lifetime of ~242 ps. In addition, a third, non-decaying component contributes to the long-lived negative signal. The negative signal is nearly zero in comparison to the initial positive peak ($\sim 3.1 \times 10^{-3}$).[69]

In stark contrast, the ΔA signal of Co–N/P-C-4 (Fig. 9b) transitions to negative values more rapidly (at ~130 ps). Additionally, in Co–N/P-C-4, the magnitude of the negative signal (-1×10^{-3} ΔA) is about one-third of the initial positive peak ($\sim 3 \times 10^{-3}$ ΔA). The kinetics graph presents three distinct lifetimes: an initial fast decay at ~235 fs, a second at ~535 ps, and a third non-decaying component contributing to the stronger persistent negative signal. The second lifetime (~535 ps) is likely due to the trapping of charge carriers, leading to the observed negative ΔA signal. This strong negative signal persists beyond the 6 ns experimental time window (*i.e.* the non-decaying component) and is attributed to the presence of trapped charge carriers.

Similarly, the ΔA signal of Fe–N/P-C-4 (Fig. 9c) also transitions to a negative ΔA signal within the same time frame. Again, this negative signal persists over the entire 6 ns detection time window and is similarly attributed to the trapping of charge

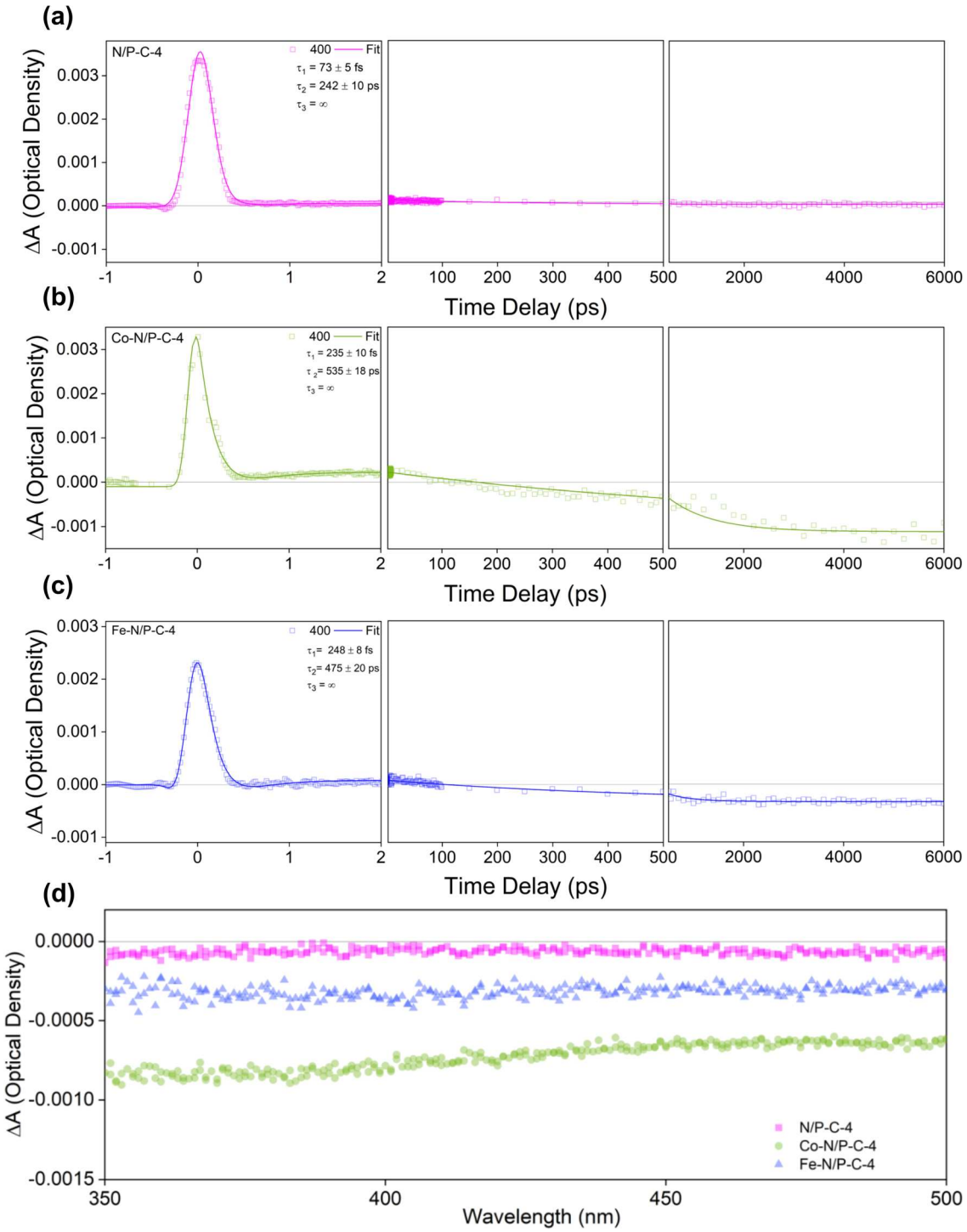

Fig. 9 Transient absorption spectroscopy (TAS) data obtained using a pump wavelength of 267 nm. (a–c) Kinetic absorption traces (ΔA) for N/P-C-4, Co–N/P-C-4 and Fe–N/P-C-4, obtained at a probe wavelength of 400 nm. To display the whole kinetics, three spectra show the signal over the 6 ns timescale for all three samples. The overlaid traces are multiexponential fits, with corresponding lifetimes (τ_1, τ_2, and τ_3). (d) Differential absorption spectra of N/P-C-4, Co–N/P-C-4 and Fe–N/P-C-4 measured 2 ns after excitation.

carriers. The kinetics graph reveals three distinct lifetimes: an initial fast component at ~248 fs, followed by a second component at ~475 ps, where charge trapping likely occurs more rapidly compared to Co–N/P-C-4, and a third non-decaying component contributing to the persistent negative signal. The initial ΔA signal reaches $\sim 3 \times 10^{-3}$ ΔA, with a subsequent negative signal of approximately -5×10^{-4} ΔA, roughly one-sixth of the positive peak. A stronger signal for the Fe-decorated sample was expected, but surprisingly, the Co-decorated sample shows a more negative signal.

The difference in magnitude of the signal could be attributed to different defect densities in the materials (*e.g.* due to differences in the ratio between metal oxide nanoparticles and single-atom Me-$N_{2/4}$ sites); or simply a slight difference between dispersion of the two samples during the experiments. Similar charge trapping dynamics, demonstrating a comparable signal, have been previously reported.[70,71] Additionally, we tested Pt/C dispersed in ethanol and observed a similar broad negative signal which further confirms that negative signal is attributed to the charge-trapping sites (Fig. S15†).

Meanwhile, the ΔA spectra of the three samples recorded 2 ns after excitation by the pump pulse are presented in Fig. 9d for direct comparison. The ΔA spectra of the three samples at 0.5 ps, 5 ps, 500 ps, and 4 ns are presented in Fig. S16(a–c)† for comparison. The relative differences in signal intensity are clearly observed, with iron and cobalt decoration resulting in significantly stronger negative signals. These are linked to charge-trapping sites (which could be associated with Fe–$N_{2/4}$ or Co–$N_{2/4}$ sites or metal oxide nanoparticles), facilitating enhanced non-radiative recombination pathways.

Discussion

The above results show that a clear difference between the metal-free nitrogen and phosphorus-doped carbons and their transition-metal decorated analogues can be observed by using time-resolved TAS. The main differences are: (i) the timescale of the transition to negative ΔA signals, and (ii) the magnitude of the negative ΔA signal after relaxation. These differences are attributed to the presence of trapping sites for excited charge carriers. The responsible charge trapping sites are posited to be either porphyrin-like metal centers (*i.e.* single metal atoms coordinated to nitrogen atoms at defects in the carbon matrix to which ORR activity is generally attributed), metal oxide nanoparticles (as observed in these samples *via* HR-TEM), or a combination of both. In the case of porphyrin-type embedded sites, the central metal ion (*i.e.* Fe or Co in this case) and the structural defects where such sites form (*e.g.*, nitrogen doped vacancies) are known charge trapping sites.[70,72–74] Meanwhile, metal oxide nanoparticles have localized surface states and defect sites (such as oxygen vacancies or under-coordinated metal atoms), which are also known to trap charge carriers.[75,76] However, TAS results reveal distinct metal-dependent charge-trapping behaviors in Fe–N/P-C and Co–N/P-C beyond what might be expected from structural factors alone. Specifically, the stronger persistent negative ΔA signal observed for Co–N/P-C-4 compared to Fe–N/P-C-4 suggests a higher density or more effective charge-trapping sites within the experimental timescale in the cobalt-decorated system. While the variation could be due to differences in defect densities and dispersion, as discussed earlier, the additional difference in the decay process could be due to the intrinsic electronic properties of metal centers. In particular, the slightly faster emergence of the negative signal and the shorter lifetime of the second decay component for Fe–N/P-C-4 reflect distinct charge relaxation pathways or differences in initial trapping kinetics. This could arise from variations in the redox properties or electronic configurations of the Fe^{2+}/Fe^{3+} and Co^{2+}/Co^{3+} centers within the M–N_x moieties, influencing the nature of carrier capture. These insights highlight how the metal identity in M–N–C electrocatalysts plays a critical role in shaping ultrafast charge dynamics. Finally, charge-trapping sites are expected to contribute to the ORR in M–N–C electrocatalysts by facilitating intermediate stabilization and charge transfer, improving the overall reaction kinetics. For example, these sites can capture and localise electrons, creating regions of high electron density that enhance the interaction with adsorbed oxygen species. This can promote the reduction of oxygen by stabilizing key intermediate species, lowering the activation barriers for the reaction steps.[77] Overall, time-resolved TAS could prove to be a powerful tool for capturing ultrafast charge dynamics, offering unique insights into how metal centers influence electron transfer in catalytic processes.

Conclusion

In this study, polyaniline-derived carbon fibers were synthesized by an oxidative polymerization method. The fibers were subsequently doped with transition metals, which led to an enhanced oxygen reduction reaction (ORR) activity in both acidic and alkaline media. Particularly, the sample exhibited comparable activity to Pt/C in an alkaline medium, with a half-wave potential of 0.84 V *vs.* RHE and an onset potential of 0.93 V *vs.* RHE. We employed time-resolved transient state absorption spectroscopy (TAS) to demonstrate that metal centers in M–N–C electrocatalysts function as charge-trapping sites, which in turn are expected to facilitate charge transfer in the ORR. This was manifested as a persistent negative ΔA signal in metal-decorated electrocatalysts (Co–N/P-C-4 and Fe–N/P-C-4) with a much larger magnitude compared with a metal-free N/P-C-4 sample. We provide a direct correlation between TAS results and ORR activity, providing a strong basis for further investigation into the underlying mechanisms. Overall, this study presents an effective strategy for synthesizing metal-decorated nitrogen-doped carbon materials from polyaniline, providing a promising approach for designing high-performance electrocatalysts.

Data availaility

The raw data supporting the findings of this study are available from the corresponding author upon reasonable request.

Author contributions

Laraib Nisar: writing – review & editing, writing – original draft, visualization, methodology, investigation, formal analysis, data curation, conceptualization. M. Irfan Maulana Kusdhany: investigation. M. Nishihara: resources. Fayyaz Hussain: investigation (theoretical calculation). Andrew D Burnett: investigation (Terahertz calculation). Stephen M. Lyth: writing – review & editing, supervision. M. Pourkashanian: supervision, project administration. M. S. Ismail: writing – review & editing, supervision, formal analysis, conceptualization. Dr Adrien P Chauvet:

writing – review & editing, supervision, formal analysis, conceptualization.

Conflicts of interest

There are no conflicts to declare.

Acknowledgements

The authors gratefully acknowledge UK's Engineering and Physical Sciences Research Council (EPSRC) for the fellowship provided to The University of Sheffield (TUoS) through its flagship Energy Institute's Doctoral Training Partnership (DTP, EP/T517835/1), the UK's Natural and Environmental Research Council (NERC, NE/T010924/1), and the Sasakawa Foundation for their financial support. The authors also extend their gratitude to the Daiwa Anglo-Japanese Foundation (ref. 13826/14659) as well as to TUoS' Energy Institute for supporting LN's research placement at Kyushu University. Accordingly, the authors are grateful to Kyushu University's NEXT-FC research center for granting access to their laboratory equipment and facilities.

References

1 M. Yang, X. Shu and J. Zhang, *ChemCatChem*, 2020, **12**, 4105–4111.
2 H. Li, S. Di, P. Niu, S. Wang, J. Wang and L. Li, *Energy Environ. Sci.*, 2022, **15**, 1601–1610.
3 Y. Yao, N. Mahmood, L. Pan, G. Shen, R. Zhang, R. Gao, F.-e. Aleem, X. Yuan, X. Zhang and J.-J. Zou, *Nanoscale*, 2018, **10**, 21327–21334.
4 S. M. Lyth and A. Mufundirwa, in *Heterogeneous Catalysts*, 2021, pp. 571–592, DOI: 10.1002/9783527813599.ch32.
5 T. Takahashi, T. Ikeda, K. Murata, O. Hotaka, H. Shigeki, Y. Tachikawa, M. Nishihara, J. Matsuda, T. Kitahara, S. M. Lyth, A. Hayashi and K. Sasaki, *J. Electrochem. Soc.*, 2022, **169**, 044523.
6 H. A. Gasteiger, S. S. Kocha, B. Sompalli and F. T. Wagner, *Appl. Catal., B*, 2005, **56**, 9–35.
7 K. Artyushkova, A. Serov, S. Rojas-Carbonell and P. Atanassov, *J. Phys. Chem. C*, 2015, **119**, 25917–25928.
8 M. David, S. M. Lyth, R. Lindner and G. F. Harrington, in *Future-Proofing Fuel Cells: Critical Raw Material Governance in Sustainable Energy*, ed. M. David, S. M. Lyth, R. Lindner and G. F. Harrington, Springer International Publishing, Cham, 2021, pp. 35–56, DOI: 10.1007/978-3-030-76806-5_3.
9 C. Chen, Y. Kang, Z. Huo, Z. Zhu, W. Huang, H. L. Xin, J. D. Snyder, D. Li, J. A. Herron, M. Mavrikakis, M. Chi, K. L. More, Y. Li, N. M. Markovic, G. A. Somorjai, P. Yang and V. R. Stamenkovic, *Science*, 2014, **343**, 1339–1343.
10 S. Guo, S. Zhang and S. Sun, *Angew. Chem., Int. Ed.*, 2013, **52**, 8526–8544.
11 Z. Song, M. Norouzi Banis, H. Liu, L. Zhang, Y. Zhao, J. Li, K. Doyle-Davis, R. Li, S. Knights, S. Ye, G. A. Botton, P. He and X. Sun, *ACS Catal.*, 2019, **9**, 5365–5374.
12 M. H. Chakrabarti, N. P. Brandon, S. A. Hajimolana, F. Tariq, V. Yufit, M. A. Hashim, M. A. Hussain, C. T. J. Low and P. V. Aravind, *J. Power Sources*, 2014, **253**, 150–166.
13 Q. Jia, N. Ramaswamy, U. Tylus, K. Strickland, J. Li, A. Serov, K. Artyushkova, P. Atanassov, J. Anibal, C. Gumeci, S. C. Barton, M.-T. Sougrati, F. Jaouen, B. Halevi and S. Mukerjee, *Nano Energy*, 2016, **29**, 65–82.
14 J. Liu, B. V. Cunning, T. Daio, A. Mufundirwa, K. Sasaki and S. M. Lyth, *Electrochim. Acta*, 2016, **220**, 554–561.
15 J. Liu, S. Yu, T. Daio, M. S. Ismail, K. Sasaki and S. M. Lyth, *J. Electrochem. Soc.*, 2016, **163**, F1049.
16 G. Wu, K. L. More, C. M. Johnston and P. Zelenay, *Science*, 2011, **332**, 443–447.
17 Q. Li, R. Cao, J. Cho and G. Wu, *Adv. Energy Mater.*, 2014, **4**, 1301415.
18 G. Wu and P. Zelenay, *Acc. Chem. Res.*, 2013, **46**, 1878–1889.
19 H. Zhang, H.-C. Chen, S. Feizpoor, L. Li, X. Zhang, X. Xu, Z. Zhuang, Z. Li, W. Hu, R. Snyders, D. Wang and C. Wang, *Adv. Mater.*, 2024, **36**, 2400523.
20 T. Zhou, W. Xu, N. Zhang, Z. Du, C. Zhong, W. Yan, H. Ju, W. Chu, H. Jiang, C. Wu and Y. Xie, *Adv. Mater.*, 2019, **31**, 1807468.
21 E. F. Holby, G. Wang and P. Zelenay, *ACS Catal.*, 2020, **10**, 14527–14539.
22 M. Primbs, Y. Sun, A. Roy, D. Malko, A. Mehmood, M.-T. Sougrati, P.-Y. Blanchard, G. Granozzi, T. Kosmala, G. Daniel, P. Atanassov, J. Sharman, C. Durante, A. Kucernak, D. Jones, F. Jaouen and P. Strasser, *Energy Environ. Sci.*, 2020, **13**, 2480–2500.
23 Y. Yang, G. Wang, S. Zhang, C. Jiao, X. Wu, C. Pan, J. Mao and Y. Liu, *ACS Appl. Mater. Interfaces*, 2024, **16**, 16224–16231.
24 T. Ikeda, M. Boero, S.-F. Huang, K. Terakura, M. Oshima, J.-i. Ozaki and S. Miyata, *J. Phys. Chem. C*, 2010, **114**, 8933–8937.
25 K. Yuan, S. Sfaelou, M. Qiu, D. Lützenkirchen-Hecht, X. Zhuang, Y. Chen, C. Yuan, X. Feng and U. Scherf, *ACS Energy Lett.*, 2018, **3**, 252–260.
26 H. Shen, E. Gracia-Espino, J. Ma, K. Zang, J. Luo, L. Wang, S. Gao, X. Mamat, G. Hu, T. Wagberg and S. Guo, *Angew. Chem., Int. Ed.*, 2017, **56**, 13800–13804.
27 C. Shao, L. Wu, H. Zhang, Q. Jiang, X. Xu, Y. Wang, S. Zhuang, H. Chu, L. Sun, J. Ye, B. Li and X. Wang, *Adv. Funct. Mater.*, 2021, **31**, 2100833.
28 Y. Li, B. Chen, X. Duan, S. Chen, D. Liu, K. Zang, R. Si, F. Lou, X. Wang, M. Rønning, L. Song, J. Luo and D. Chen, *Appl. Catal., B*, 2019, **249**, 306–315.
29 Y. Zhou, R. Lu, X. Tao, Z. Qiu, G. Chen, J. Yang, Y. Zhao, X. Feng and K. Müllen, *J. Am. Chem. Soc.*, 2023, **145**, 3647–3655.
30 M. Li, T. Liu, X. Bo, M. Zhou, L. Guo and S. Guo, *Nano Energy*, 2017, **33**, 221–228.
31 E. Gracia-Espino, *J. Phys. Chem. C*, 2016, **120**, 27849–27857.
32 K. Yuan, D. Lützenkirchen-Hecht, L. Li, L. Shuai, Y. Li, R. Cao, M. Qiu, X. Zhuang, M. K. H. Leung, Y. Chen and U. Scherf, *J. Am. Chem. Soc.*, 2020, **142**, 2404–2412.

33 G. R. Lee, J. Kim, D. Hong, Y. J. Kim, H. Jang, H. J. Han, C.-K. Hwang, D. Kim, J. Y. Kim and Y. S. Jung, *Nat. Commun.*, 2023, **14**, 5402.
34 W. Zhou, B. Li, X. Liu, J. Jiang, S. Bo, C. Yang, Q. An, Y. Zhang, M. A. Soldatov, H. Wang, S. Wei and Q. Liu, *Nat. Commun.*, 2024, **15**, 6650.
35 R. Berera, R. van Grondelle and J. T. M. Kennis, *Photosynth. Res.*, 2009, **101**, 105–118.
36 R. J. Lanzafame, *Photomed. Laser Surg.*, 2007, **25**, 58.
37 S. Park, A. L. Fischer, C. J. Steen, M. Iwai, J. M. Morris, P. J. Walla, K. K. Niyogi and G. R. Fleming, *J. Am. Chem. Soc.*, 2018, **140**, 11965–11973.
38 D. Paleček, G. Tek, J. Lan, M. Iannuzzi and P. Hamm, *J. Phys. Chem. Lett.*, 2018, **9**, 1254–1259.
39 D. R. Bacon, A. D. Burnett, M. Swithenbank, C. Russell, L. Li, C. D. Wood, J. Cunningham, E. H. Linfield, A. G. Davies, P. Dean and J. R. Freeman, *Opt. Express*, 2016, **24**, 26986–26997.
40 J. Neu and C. A. Schmuttenmaer, *J. Appl. Phys.*, 2018, **124**, 231101.
41 T. Takahashi, Y. Kokubo, K. Murata, O. Hotaka, S. Hasegawa, Y. Tachikawa, M. Nishihara, J. Matsuda, T. Kitahara, S. M. Lyth, A. Hayashi and K. Sasaki, *Int. J. Hydrogen Energy*, 2022, **47**, 41111–41123.
42 C. Wei, R. R. Rao, J. Peng, B. Huang, I. E. L. Stephens, M. Risch, Z. J. Xu and Y. Shao-Horn, *Adv. Mater.*, 2019, **31**, 1806296.
43 J. Zhang, Z. Zhao, Z. Xia and L. Dai, *Nat. Nanotechnol.*, 2015, **10**, 444–452.
44 P. A. van Aken and B. Liebscher, *Phys. Chem. Miner.*, 2002, **29**, 188–200.
45 H. Wang, W. Wang, Y. Y. Xu, S. Dong, J. Xiao, F. Wang, H. Liu and B. Y. Xia, *ACS Appl. Mater. Interfaces*, 2017, **9**, 10610–10617.
46 Z. Wang, W. Xu, X. Chen, Y. Peng, Y. Song, C. Lv, H. Liu, J. Sun, D. Yuan, X. Li, X. Guo, D. Yang and L. Zhang, *Adv. Funct. Mater.*, 2019, **29**, 1902875.
47 Y. Xia, J. M. Wiesinger, A. G. MacDiarmid and A. J. Epstein, *Chem. Mater.*, 1995, **7**, 443–445.
48 S. Bhadra, N. K. Singha and D. Khastgir, *J. Appl. Polym. Sci.*, 2007, **104**, 1900–1904.
49 L. Li, Z.-Y. Qin, X. Liang, Q.-Q. Fan, Y.-Q. Lu, W.-H. Wu and M.-F. Zhu, *J. Phys. Chem. C*, 2009, **113**, 5502–5507.
50 C. V. Rao, C. R. Cabrera and Y. Ishikawa, *J. Phys. Chem. Lett.*, 2010, **1**, 2622–2627.
51 L. Qu, Y. Liu, J.-B. Baek and L. Dai, *ACS Nano*, 2010, **4**, 1321–1326.
52 A. Samadi, Z. Wang, S. Wang, S. K. Nataraj, L. Kong and S. Zhao, *Chem. Eng. J.*, 2023, **478**, 147506.
53 K. Lee, S. Cho, S. Heum Park, A. J. Heeger, C.-W. Lee and S.-H. Lee, *Nature*, 2006, **441**, 65–68.
54 J. W. F. To, Z. Chen, H. Yao, J. He, K. Kim, H.-H. Chou, L. Pan, J. Wilcox, Y. Cui and Z. Bao, *ACS Cent. Sci.*, 2015, **1**, 68–76.
55 Z. Wang, Z. Lu, Q. Ye, Z. Yang, R. Xu, K. Kong, Y. Zhang, T. Yan, Y. Liu, Z. Pan, Y. Huang and X. Lu, *Adv. Funct. Mater.*, 2024, **34**, 2315150.
56 F. Wu, J. Li, Y. Tian, Y. Su, J. Wang, W. Yang, N. Li, S. Chen and L. Bao, *Sci. Rep.*, 2015, **5**, 13340.
57 H. J. Kim, S. Im, J. C. Kim, W. G. Hong, K. Shin, H. Y. Jeong and Y. J. Hong, *ACS Sustain. Chem. Eng.*, 2017, **5**, 6654–6664.
58 J. Zhang, J. Jiang, H. Li and X. S. Zhao, *Energy Environ. Sci.*, 2011, **4**, 4009–4015.
59 X. Cui, Q. Li, Y. Li, F. Wang, G. Jin and M. Ding, *Appl. Surf. Sci.*, 2008, **255**, 2098–2103.
60 T. Y. Ma, J. Ran, S. Dai, M. Jaroniec and S. Z. Qiao, *Angew. Chem., Int. Ed.*, 2015, **54**, 4646–4650.
61 Z.-H. Sheng, L. Shao, J.-J. Chen, W.-J. Bao, F.-B. Wang and X.-H. Xia, *ACS Nano*, 2011, **5**, 4350–4358.
62 H. B. Yang, J. Miao, S.-F. Hung, J. Chen, H. B. Tao, X. Wang, L. Zhang, R. Chen, J. Gao, H. M. Chen, L. Dai and B. Liu, *Sci. Adv.*, 2016, **2**, e1501122.
63 Y. Tong, P. Chen, T. Zhou, K. Xu, W. Chu, C. Wu and Y. Xie, *Angew. Chem., Int. Ed.*, 2017, **56**, 7121–7125.
64 H. Tabassum, W. Guo, W. Meng, A. Mahmood, R. Zhao, Q. Wang and R. Zou, *Adv. Energy Mater.*, 2017, **7**, 1601671.
65 D. M. Morales, M. A. Kazakova, S. Dieckhöfer, A. G. Selyutin, G. V. Golubtsov, W. Schuhmann and J. Masa, *Adv. Funct. Mater.*, 2020, **30**, 1905992.
66 P. A. Obraztsov, M. G. Rybin, A. V. Tyurnina, S. V. Garnov, E. D. Obraztsova, A. N. Obraztsov and Y. P. Svirko, *Nano Lett.*, 2011, **11**, 1540–1545.
67 A. W. Rokmana, A. Asriani, H. Suhendar, K. Triyana, A. Kusumaatmaja and I. Santoso, *J. Phys.: Conf. Ser.*, 2018, **1011**, 012007.
68 J. Shang, T. Yu, J. Lin and G. G. Gurzadyan, *ACS Nano*, 2011, **5**, 3278–3283.
69 A. J. Auty, N. Mansouriboroujeni, T. Nagaraja, D. Chekulaev, C. M. Sorensen, S. R. Das, N. Martsinovich and A. A. P. Chauvet, *J. Phys. Chem. C*, 2022, **126**, 7949–7955.
70 S. Kaniyankandy, S. N. Achary, S. Rawalekar and H. N. Ghosh, *J. Phys. Chem. C*, 2011, **115**, 19110–19116.
71 T. V. Alencar, M. G. Silva, L. M. Malard and A. M. de Paula, *Nano Lett.*, 2014, **14**, 5621–5624.
72 R. Godin, Y. Wang, M. A. Zwijnenburg, J. Tang and J. R. Durrant, *J. Am. Chem. Soc.*, 2017, **139**, 5216–5224.
73 M. He, X. Wang, H. Yu, Y. Zhao, L. Zhang, Z. Xu, Y. Kang and P. Xue, *Biomaterials*, 2024, **305**, 122446.
74 M. Qian, X.-L. Wu, M. Lu, L. Huang, W. Li, H. Lin, J. Chen, S. Wang and X. Duan, *Adv. Funct. Mater.*, 2023, **33**, 2208688.
75 I. Chakraborty, S.-N. Lai, M.-C. Wu, H.-Y. Lin, C. Li, J. M. Wu and C.-S. Lai, *Mater. Horiz.*, 2021, **8**, 3149–3162.
76 A. Kafizas, R. Godin and J. R. Durrant, in *Semiconductors and Semimetals*, ed. Z. Mi, L. Wang and C. Jagadish, Elsevier, 2017, vol. 97, pp. 3–46.
77 Z. Li, H. Cheng, Y. Lu, T. Wang, Y. Li, W. Zhang, G. He and Z. Tian, *Adv. Energy Mater.*, 2023, **13**, 2203963.